Editors' Suggestion

# Trapped waves on interfacial hydraulic falls over bottom obstacles

Z. Wang* and J. Chai
*Institute of Mechanics, Chinese Academy of Sciences, Beijing 100190, People's Republic of China and School of Engineering Science, University of Chinese Academy of Sciences, Beijing 100049, People's Republic of China*

E. I. Părău† and C. Page
*School of Mathematics, University of East Anglia, Norwich NR4 7TJ, United Kingdom*

M. Wang‡
*Beijing Institute of Control Engineering, Beijing 100190, People's Republic of China*

(Received 2 April 2022; accepted 27 May 2022; published 1 July 2022)

Hydraulic falls on the interface of a two-layer density stratified fluid flow in the presence of bottom topography are considered. We extend the previous work [Philos. Trans. R. Soc. London A **360**, 2137 (2002)] to two successive bottom obstructions of arbitrary shape. The forced Korteweg-de Vries and modified Korteweg-de Vries equations are derived in different asymptotic limits to understand the existence and classification of fall solutions. The full Euler equations are numerically solved by a boundary integral equation method. New solutions characterized by a train of trapped waves are found for interfacial flows past two obstacles. The wavelength of the trapped waves agrees well with the prediction of the linear dispersion relation. In addition, the effects of the relative location, aspect ratio, and convexity-concavity property of the obstacles on interface profiles are investigated.

DOI: 10.1103/PhysRevFluids.7.074801

## I. INTRODUCTION

The problem of a constant-moving flow over a bottom obstacle in an open channel has a long history in hydrodynamics. Studies of the existence and stability of steady solutions are an important step toward understanding the whole problem. For free surface flows over a single localized obstacle, solutions depend on the Froude number $F$, defined as $F = U/\sqrt{gH}$, where $U$ is the uniform upstream/downstream velocity of the fluid, $H$ denotes the uniform upstream/downstream fluid depth, and $g$ is the acceleration due to gravity. The uniform flow at infinity is called supercritical for $F > 1$ and subcritical for $F < 1$. Four basic flows were identified by Dias and Vanden-Broeck [1]: supercritical flow on both sides, subcritical flow upstream and waves downstream, subcritical flow upstream and supercritical flow downstream (hydraulic fall), and waves upstream and supercritical flow downstream (generalized hydraulic fall). The first three types of solution in the steady Euler equations have been numerically studied previously by many groups. Forbes and Schwartz [2] computed the first two types of solution in the presence of a semicircular obstruction. Vanden-Broeck [3] further explored the first type and found that supercritical solutions can exist only for values of the Froude number greater than some threshold. And for some Froude numbers, there are two solutions,

*zwang@imech.ac.cn
†e.parau@uea.ac.uk
‡wangmian_imech@163.com

 

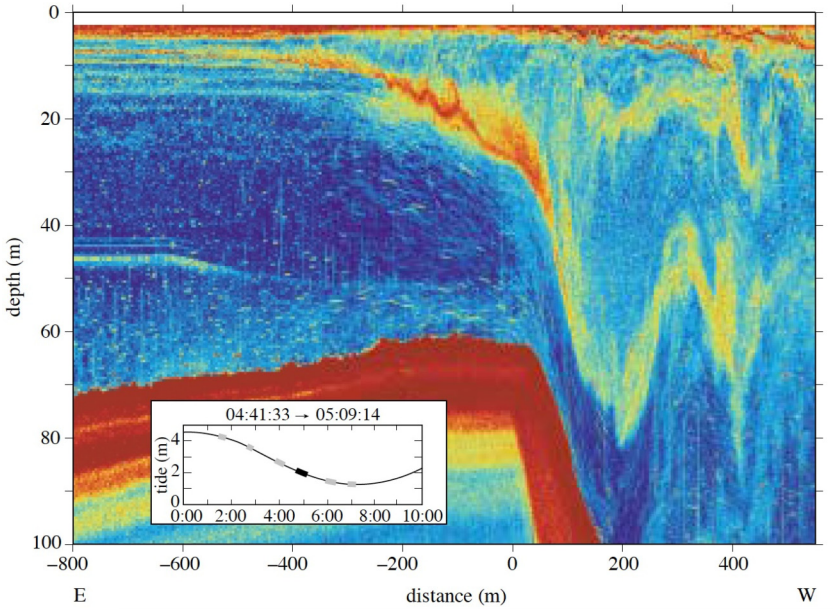


FIG. 1. A field observation of internal hydraulic jump obtained by Farmer and Armi near the sill in Knight Inlet in autumn 1995 (see Fig. 7(d) in Ref. [11]).

one being a perturbation of a uniform stream and the other being a perturbation of a solitary wave. In the nearly critical regime, hydraulic falls were calculated by Forbes [4], who found that as the radius of the submerged obstacle is increased, the speed of the downstream portion of the flow increases, with a consequent reduction in the upstream Froude number. For a submerged triangular obstacle, Dias and Vanden-Broeck [5] studied waves of permanent form without oscillation in the far-field, and they found that solutions exist for triangles of arbitrary size.

Solutions of the fourth type were computed by Dias and Vanden-Broeck [6]; however, as they pointed out, the generalized hydraulic falls lack physical meaning because waves on the free surface do not satisfy the radiation condition. Nevertheless, Dias and Vanden-Broeck [1] argued that the radiation condition could be satisfied by introducing a second obstacle in the channel. Therefore these generalized hydraulic falls can be used to describe locally the flow past two successive obstacles resulting in trapped waves. Shortly after, Binder *et al.* [7] revisited the same problem and discovered more configurations of hydraulic falls with trapped waves between submerged obstacles and forced solitary waves through weakly nonlinear analysis and numerical computations of the fully nonlinear equations. Page and Părău [8] examined the stability property of gravity trapped waves upstream of a hydraulic fall using direct numerical simulations for the unsteady Euler equations, indicating that they are stable. When other restoring forces are included in addition to gravity, trapped waves between two submerged obstructions were later investigated by Page *et al.* [9,10] for capillary-gravity waves and flexural-gravity waves, respectively.

Hydraulic falls occurring in the interiors of oceans as stratified tidal flows pass sills or submarine ridges also attract research attention due to their associations with ocean mixing as well as the generation of nonlinear internal waves or wave trains (see Ref. [11], for example). Figure 1 shows the field observation of a stratified flow over topography in Knight Inlet (British Columbia, Canada) measured by Farmer and Armi [11], illustrating the downstream formation of an undular internal hydraulic jump. A simple mathematical idealization for studying internal waves is the wave propagation on the sharp density discontinuity between two immiscible fluids. Under this simplification, interfacial hydraulic falls have been considerably investigated in numerics, theory,

and experiment over the past several decades. The first interfacial waterfall-like solution over a semicircle obstruction was numerically found in the full Euler equations by Forbes [12] in the transcritical regime based on the conformal mapping technique. For the same problem, Sha and Vanden-Broeck [13] computed forced interfacial solitary waves based on a novel boundary integral equation method with the arclength parametrization of the interface and found two limiting configurations: broadening and overhanging. On the theoretical side, Shen [14] used a forced Korteweg-de Vries (KdV) equation to obtain solitary and hydraulic solutions for two-layer flows over a bottom obstruction. Notably, he allowed the upper layer to be bounded above by a free surface rather than a rigid lid. Dias and Vanden-Broeck [15,16] combined theory and computation, i.e., the weakly nonlinear results obtained by integrating the forced KdV equation or the forced modified Korteweg-de Vries (mKdV) equation are validated by comparison with numerical results obtained by solving the full Euler equations. Consequently, they found new branches of solutions akin to the single-layer situation. Moreover, considerable understanding of two-layer flow over an obstacle was also gained from controlled experiments, notably the towing-tank experiments of Long [17] and Baines [18] and the fixed-obstacle experiments of Lawrence [19]. It is also worth mentioning that when the bottom obstacle is of significant height, a situation occasionally encountered in real ocean flows, the forced KdV theory no longer applies, so numerical and experimental studies were carried out to investigate those cases. For example, Cummins *et al.* [20] and Cabeza *et al.* [21] performed experimental measurements for two-layer flows past pronounced obstacles and simulated the observed phenomena using the incompressible Navier-Stokes equation with Boussinesq approximation for buoyancy terms.

Though Dias and Vanden-Broeck [15,16] conducted extensive numerical simulations on steady interfacial hydraulic falls, computations of two-layer flows past two successive obstacles and the resultant trapped interfacial waves remain lacking. Furthermore, the effect of the combination mode of two obstructions (convex or concave) at the bottom merits an investigation. In the present paper, we report numerical results of steady hydraulic falls for two-layer flow over bottom obstacles and pay particular attention to trapped waves between two obstructions. Direct numerical computations of the primitive Euler equations are performed based on the boundary integral equation method proposed by Belward and Forbes [22], a scheme applicable to arbitrary bottom topography. Our numerical results also confirm the predictions of the weakly nonlinear theory.

The rest of the article is structured as follows. The mathematical formulation of the problem is described in Sec. II. The theoretical results are presented in Sec. III, including the linear dispersion relation and the weakly nonlinear theory leading to the forced KdV equation and the forced mKdV equation based on the small-amplitude assumption on both interface and obstacle. Section IV begins with computations of interfacial hydraulic falls over a single obstacle in the full Euler equations. The goal is threefold: to validate the numerical scheme of the boundary integral formulation, to understand the influence of obstacle's aspect ratio on falls, and to gain iterative initial data of Newton's method for computations of trapped waves. Next, trapped interfacial waves between two obstacles of different aspect ratios and combination modes are numerically solved, where the predictions of the KdV theory are used to guide the computations of the fully nonlinear equations. Finally, a conclusion is given in Sec. V.

## II. DESCRIPTIONS OF PROBLEM

Two inviscid, incompressible, and immiscible fluids are bounded together in a two-dimensional channel of finite vertical extent and infinite horizontal extent. A sketch of the system is shown in Fig. 2. The top boundary is flat, and the topographic relief at the bottom is locally confined. We introduce a Cartesian coordinate system such that the $x$ axis is parallel to the rigid top wall and the $y$ axis is parallel to the opposite direction of gravity. We denote by $y = H_1 + H_2$ and $y = b(x)$ the upper and lower boundaries, respectively, where $b(x)$ is a function with compact support. The interface between two fluids is denoted as $y = H_1 + \zeta(x)$. The subscripts 1 and 2 refer to fluid properties associated with the lower and upper fluid layers, respectively. The fluid density in each

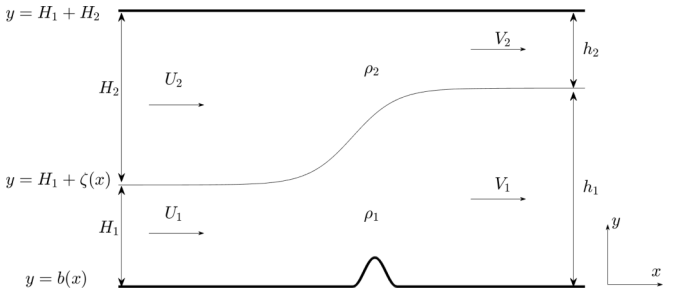


FIG. 2. Schematic description of the physical problem.

layer is supposed to be constant, designated by $\rho_j$ ($j = 1, 2$), and the system is in a stable density configuration, namely $\rho_2 < \rho_1$. The depth of each layer at infinity is denoted by $H_j$ for upstream and $h_j$ for downstream. The upstream and downstream velocities are supposed to be uniform and are designated as $U_j$ and $V_j$, respectively.

The motion of each fluid is assumed to be irrotational; thus, we can introduce velocity potentials $\phi_1$ and $\phi_2$, which satisfy the Laplace equation in the corresponding layers, namely

$$\phi_{1xx} + \phi_{1yy} = 0, \quad \text{for } b(x) < y < H_1 + \zeta(x), \tag{1}$$

$$\phi_{2xx} + \phi_{2yy} = 0, \quad \text{for } H_1 + \zeta(x) < y < H_1 + H_2. \tag{2}$$

The impermeability boundary conditions at the top and bottom are written as

$$\phi_{1y} = \phi_{1x} b_x, \quad \text{at } y = b(x), \tag{3}$$

$$\phi_{2y} = 0, \quad \text{at } y = H_1 + H_2. \tag{4}$$

Since we search for steady solutions in the present paper, the kinematic boundary conditions at the interface can be written as

$$0 = \phi_{1y} - \phi_{1x}\zeta_x = \phi_{2y} - \phi_{2x}\zeta_x, \quad \text{at } y = H_1 + \zeta(x), \tag{5}$$

indicating the continuity of normal velocity across the media. The dynamic boundary condition resulting from the continuity of pressure across the interface reads

$$\tfrac{1}{2}\left[\rho_1\left(\phi_{1x}^2 + \phi_{1y}^2\right) - \rho_2\left(\phi_{2x}^2 + \phi_{2y}^2\right)\right] + g(\rho_1 - \rho_2)\zeta - \tfrac{1}{2}\left(\rho_1 U_1^2 - \rho_2 U_2^2\right) = 0, \tag{6}$$

where the Bernoulli constants at infinity are used. In addition, conservations of mass and height yield

$$H_1 + H_2 = h_1 + h_2, \quad U_1 H_1 = V_1 h_1, \quad U_2 H_2 = V_2 h_2. \tag{7}$$

Equations (1)–(7) form a closed system for steady internal hydraulic falls. Finally, for the convenience of later discussion, we introduce dimensionless parameters including the density ratio, depth ratio, velocity ratios, Froude numbers upstream, and Froude numbers downstream as

$$R = \frac{\rho_2}{\rho_1}, \quad \Theta = \frac{H_2}{H_1}, \quad \beta = \frac{U_2}{U_1}, \quad \beta_1 = \frac{V_1}{U_1}, \quad \beta_2 = \frac{V_2}{U_2},$$
$$F_{1u} = \frac{U_1}{\sqrt{gH_1}}, \quad F_{2u} = \frac{U_2}{\sqrt{gH_2}}, \quad F_{1d} = \frac{V_1}{\sqrt{gh_1}}, \quad F_{2d} = \frac{V_2}{\sqrt{gh_2}},$$

where the subscripts $u$ and $d$ refer to the parameters associated with the flows upstream and downstream, respectively.

## III. THEORETICAL ANALYSIS

### A. Linear analysis

In the subsequent analyses, we investigate the problem from the linear perspective. First, the smallness assumption is made on wave amplitude, $\zeta/H_1 \sim \mathcal{O}(\epsilon)$, and on bottom topography, $b/H_1 \sim \mathcal{O}(\epsilon^2)$, where $\epsilon \ll 1$ is a small parameter. We then linearize the whole system around the trivial solution $\phi_j = U_j x$ and $\zeta = 0$. The perturbations of velocity potentials and interface are chosen to be expressed in the form of separated variables, i.e.,

$$\zeta = \epsilon\,\widehat{\zeta}\,e^{ikx}, \quad \phi_j = U_j x + \epsilon\,\widehat{\phi}_j(y)\,e^{ikx}, \tag{8}$$

where $j = 1, 2$ and $k$ is the wave number. Next, we drop nonlinear terms in Eqs. (1)–(7) and solve the problem in a uniform channel. Substituting the solution ansatz into the Laplace equations (1) and (2) and the impermeability boundary conditions (3) and (4), one obtains

$$\widehat{\phi}_1 = \alpha\cosh(ky), \quad \widehat{\phi}_2 = -\alpha\beta\,\frac{\sinh(kH_1)}{\sinh(kH_2)}\cosh(kH_1 + kH_2 - ky), \tag{9}$$

where $\alpha$ is a free parameter. Furthermore, using the kinematic boundary conditions at the interface, $\zeta$ can be solved as

$$\zeta = \frac{\epsilon\alpha}{iU_1}\sinh(kH_1)\,e^{ikx}. \tag{10}$$

Then, substituting the expressions of $\phi_j$ and $\zeta$ into the linearized dynamic boundary condition yields a linear dispersion relation

$$F_{1u}^2 = \frac{(1-R)\tanh(K)\tanh(\Theta K)}{K\tanh(\Theta K) + R\beta^2 K\tanh(K)}, \tag{11}$$

where $K = kH_1$ is the normalized wave number. The critical Froude number for the lower-layer upstream can be defined by taking the limit $K \to 0$, i.e.,

$$F_{1u}^{*\,2} = \frac{\Theta(1-R)}{\Theta + R\beta^2}. \tag{12}$$

A similar derivation can be applied to the quantities downstream, and the dispersion relation reads

$$F_{1d}^2 = \frac{(1-R)\tanh\left(\frac{K}{\beta_1}\right)\tanh\left(\frac{\Theta K}{\beta_2}\right)}{\frac{K}{\beta_1}\tanh\left(\frac{\Theta K}{\beta_2}\right) + R\beta^2 K\frac{\beta_2^2}{\beta_1^3}\tanh\left(\frac{K}{\beta_1}\right)}, \tag{13}$$

where $K = kh_1$ is the corresponding wave number. It is noted that the dispersion relations (11) and (13) will be used later to estimate the wavelength of trapped waves between two obstacles.

### B. Weakly nonlinear analysis

In this part, the forced KdV-type models are derived via asymptotic analyses in the long-wave approximation. These models will be used in the next section to guide numerical computations of the full Euler equations and provide qualitative understandings of interfacial hydraulic falls. Our analyses are based on a fundamental assumption that both fluid layers are thin compared with a characteristic wavelength. Small parameters $\epsilon = a/H_1 \ll 1$ and $\mu = H_1/l \ll 1$ are defined to measure the nonlinearity and dispersion, respectively, where $l$ is a characteristic wavelength in the $x$ direction and $a$ is a typical amplitude of the interface displacement. We consider the classic Boussinesq scaling:

$$x = lx', \quad y = H_1 y', \quad \zeta = a\zeta', \quad b = \epsilon^2 H_1 b', \quad U_1 = \sqrt{gH_1}F_{1u}, \quad U_2 = \sqrt{gH_1}F_{1u}\beta,$$
$$\phi_1 = \sqrt{gH_1}F_{1u}lx' + \frac{agl}{\sqrt{gH_1}}\phi_1', \quad \phi_2 = \sqrt{gH_1}F_{1u}\beta lx' + \frac{agl}{\sqrt{gH_1}}\phi_2'.$$

It is noted that velocity potentials have been expressed as a sum of a background flow and its perturbation. Using these dimensionless variables and dropping the apostrophes for the ease of notations, the field equations and the wall boundary conditions become

$$\begin{aligned} \mu^2\phi_{1xx} + \phi_{1yy} &= 0, \quad \text{for } 0 < y < 1 + \epsilon\zeta, \\ \mu^2\phi_{2xx} + \phi_{2yy} &= 0, \quad \text{for } 1 + \epsilon\zeta < y < 1 + \Theta, \\ \phi_{1y} &= \epsilon\mu^2 F_{1u} b_x + \epsilon^2\mu^2\phi_{1x}b_x, \quad \text{at } y = \epsilon^2 b, \\ \phi_{2y} &= 0, \quad \text{at } y = 1 + \Theta. \end{aligned} \tag{14}$$

At the same time, the kinematic and dynamic boundary conditions at the interface $y = 1 + \epsilon\zeta$ are recast to

$$0 = \mu^2 F_{1u}\zeta_x + \epsilon\mu^2\phi_{1x}\zeta_x - \phi_{1y} = \mu^2 F_{1u}\beta\zeta_x + \epsilon\mu^2\phi_{2x}\zeta_x - \phi_{2y}, \tag{15}$$

$$0 = \frac{1}{2}\left[2F_{1u}\phi_{1x} + \epsilon\phi_{1x}^2 + \frac{\epsilon}{\mu^2}\phi_{1y}^2 - R\left(2\beta F_{1u}\phi_{2x} + \epsilon\phi_{2x}^2 + \frac{\epsilon}{\mu^2}\phi_{2y}^2\right)\right] + \zeta(1 - R). \tag{16}$$

Small parameters are chosen to satisfy $\epsilon = \mu^2$ to balance dispersion and nonlinearity. Based on the system (14), we can write the asymptotic expansions of $\phi_1$ and $\phi_2$ as

$$\phi_1 = f_1(x) - \frac{\epsilon}{2}f_{1xx}y^2 + \frac{\epsilon^2}{24}f_{1xxxx}y^4 + \epsilon^2 F_{1u}b_x y + \mathcal{O}(\epsilon^3), \tag{17}$$

$$\phi_2 = f_2(x) - \frac{\epsilon}{2}f_{2xx}(y - 1 - \Theta)^2 + \frac{\epsilon^2}{24}f_{2xxxx}(y - 1 - \Theta)^4 + \mathcal{O}(\epsilon^3), \tag{18}$$

where $f_1(x)$ and $f_2(x)$ are the velocity potentials at the bottom and top walls, respectively. Substituting the expressions (17) and (18) into Eqs. (15) and (16) and retaining terms valid up to the next-to-leading order for each equation, one obtains

$$\zeta_x + \frac{1}{F_{1u}}f_{1xx} + \frac{\epsilon}{F_{1u}}\left(f_{1x}\zeta_x + f_{1xx}\zeta - \frac{1}{6}f_{1xxxx}\right) = \epsilon b_x, \tag{19}$$

$$\beta\zeta_x - \frac{\Theta}{F_{1u}}f_{2xx} + \frac{\epsilon}{F_{1u}}\left(f_{2x}\zeta_x + f_{2xx}\zeta - \frac{\Theta^3}{6}f_{2xxxx}\right) = 0, \tag{20}$$

$$\frac{1 - R}{F_{1u}}\zeta + f_{1x} - R\beta f_{2x} + \epsilon\left(\frac{1}{2}f_{1xxx} + \frac{R\beta\Theta^2}{2}f_{2xxx} + \frac{1}{2F_{1u}}f_{1x}^2 - \frac{R}{2F_{1u}}f_{2x}^2\right) = 0. \tag{21}$$

First, the solvability condition for the linearized system of (19)–(21) indicates $F_{1u} = F_{1u}^* + \epsilon\lambda$, where $\lambda = O(1)$ is a newly introduced parameter. Then it is a little tedious but straightforward to convert (19)–(21) to a single equation, the steady forced KdV equation. Eliminating $f_1$ and $f_2$ in Eq. (21) by virtue of (19)–(20) and retaining terms valid up to $O(\epsilon)$, one obtains

$$-\frac{\Theta}{2(\Theta + R\beta^2)}b_x = -\frac{\lambda}{F_{1u}^*}\zeta_x + \frac{3}{2}\frac{\Theta^2 - R\beta^2}{\Theta(\Theta + R\beta^2)}\zeta\zeta_x + \frac{1}{6}\frac{\Theta(1 + R\beta^2\Theta)}{\Theta + R\beta^2}\zeta_{xxx}, \tag{22}$$

which can be transformed to the standard form

$$-\tfrac{1}{2}b_x = -\lambda\zeta_x \pm \tfrac{3}{2}\zeta\zeta_x + \tfrac{1}{6}\zeta_{xxx}. \tag{23}$$

The derivation is rather standard, and the interested readers are referred to Ref. [23] for more details. If we assume the topography $b(x)$ is a Dirac $\delta$ function of weight $Q$, namely $b(x) = Q\delta(x)$, then integrating Eq. (23) yields

$$\zeta_{xx} \pm \tfrac{9}{2}\zeta^2 - 6\lambda\zeta = -3Q\delta. \tag{24}$$

Again, integrating Eq. (24) over a small interval including the original point, from $-\varepsilon$ to $\varepsilon$ with $\varepsilon \to 0$, say, gives

$$\zeta_x(0^+) - \zeta_x(0^-) = -3Q, \tag{25}$$

indicating that the derivative of the interface features a jump at the position of the bottom obstruction. Furthermore, letting $A = \zeta$ and $B = \zeta_x$, solutions to the homogenous KdV equation ($Q = 0$) can be described by an autonomous system,

$$\frac{dA}{dx} = B, \quad \frac{dB}{dx} = \mp\frac{9}{2}A^2 + 6\lambda A, \tag{26}$$

with two equilibrium/saddle points: $\zeta = 0$ and $\zeta = \pm\frac{4}{3}\lambda$.

It is well known that the KdV equation is obtained by balancing dispersive and nonlinear effects. However, when $\Theta \approx \sqrt{R\beta^2}$, the nonlinear term is very close to zero, and hence rescaling is required in the asymptotic analysis to achieve a new balance. Under this particular situation, we should choose $\epsilon = \mu$ and assume $R\beta^2 = \Theta^2 + \epsilon\sigma$, $F_{1u} = F_{1u}^* + \epsilon^2\lambda$, and $b = \epsilon^3 H_1 b'$ to introduce a higher-order nonlinearity to balance the dispersion (see, for example, Ref. [16] for more details). Following a similar asymptotic procedure, a forced mKdV equation including the cubic nonlinearity can be obtained

$$-\frac{b_x}{2(1+\Theta)} = -\frac{\lambda}{F_{1u}^*}\zeta_x + \frac{3\sigma}{\Theta^2+\Theta}\zeta\zeta_x - \frac{3(1-\Theta)}{\Theta^2+\Theta}\zeta^2\zeta_x + \frac{1-\Theta+\Theta^2}{6}\zeta_{xxx}. \tag{27}$$

The above equation can be rewritten in a more revealing form via rescaling,

$$-\tfrac{1}{2}b_x = -\lambda\zeta_x + \tfrac{3}{2}\sigma\zeta\zeta_x - \tfrac{3}{4}\zeta^2\zeta_x + \tfrac{1}{6}\gamma\zeta_{xxx}, \tag{28}$$

where $\gamma = (1 - \Theta + \Theta^2)F_{1u}^*$. By neglecting the external forcing, the dynamical system has three equilibrium/saddle points, $\zeta = 0$ and $\zeta = \frac{3}{2}\sigma \pm \frac{1}{2}\sqrt{9\sigma^2 - 16\lambda}$, when $\lambda < \frac{16}{9}\sigma^2$. However, the number of the equilibrium points reduces to two and one for $\lambda = \frac{16}{9}\sigma^2$ and $\lambda > \frac{16}{9}\sigma^2$, respectively.

We emphasize that the weakly nonlinear results described in this section are not new but are included here for completeness (see Refs. [15,16]). The hydraulic solutions can be divided into six categories in terms of $F_{1u}$ and $\Theta$. The flow upstream can be subcritical if $F_{1u} < F_{1u}^*$ or supercritical if $F_{1u} > F_{1u}^*$. We define a case as the "thick upper layer" for $\Theta > \sqrt{\beta^2 R}$, the "thick lower layer" for $\Theta < \sqrt{\beta^2 R}$, and the critical case for $\Theta = \sqrt{\beta^2 R}$. This paper is primarily devoted to the numerical evidence and basic properties of interfacial hydraulic falls. Using a phase diagram of $(\lambda, Q)$ of the KdV equation, Dias and Vanden-Broeck show that the hydraulic solutions exist only when $|Q| = \frac{4}{9}\sqrt{2}|\lambda|^{3/2}$ (see Ref. [15]). Their theoretical prediction classifies the solutions and associates each with a corresponding region. In this paper, the parameter $\beta$ is fixed as $\beta = 1$, and we focus on far-field wave-free solutions. Four typical regimes will be considered, and they are denoted as follows: Regime (I) subcritical flow upstream and thick upper layer; Regime (II) supercritical flow upstream and thick upper layer; Regime (III) subcritical flow upstream and thick bottom layer; and Regime (IV) subcritical flow upstream and critical depth. Finally, we should point out that we did not manage to find the numerical solutions in the full Euler equations for the other two cases, namely supercritical flow upstream with a critical depth and supercritical flow upstream with a thick bottom layer, which are left for future studies.

## IV. NUMERICAL RESULTS

### A. Numerical scheme

The fully nonlinear problem can be numerically solved by using the boundary integral equation method with the arclength parametrization of the interface. This numerical scheme was first proposed by Forbes and Schwartz in Ref. [2] and was widely used to search for steady hydraulic falls on the water surface. We briefly introduce the numerical scheme, and the interested readers

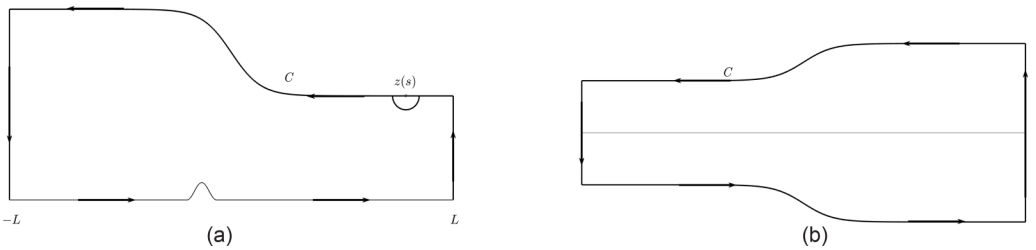


FIG. 3. Sketch of the contour of integration (a) for the lower fluid and (b) for the upper fluid.

are referred to Refs. [16,22] for more details. It is convenient to choose $H_1$ and $H_1U_1$ as the units of length and velocity potential, respectively. Following Ref. [22], the fluid interface is first parametrized by writing $x = X(s)$ and $y = 1 + \zeta(x) = Y(s)$ so that the following condition is satisfied automatically:

$$\left(\frac{dX}{ds}\right)^2 + \left(\frac{dY}{ds}\right)^2 = 1. \tag{29}$$

Thus the parameterized dynamic boundary condition can be rewritten as

$$\frac{1}{2}\left(\frac{d\phi_1}{ds}\right)^2 - \frac{R}{2}\left(\frac{d\phi_2}{ds}\right)^2 - \frac{1}{2}(1 - R\beta^2) + \frac{1}{F_1^2}(1 - R)(Y - 1) = 0. \tag{30}$$

Second, we introduce the complex velocity potential $w_j(z) = \phi_j(x, y) + i\psi_j(x, y)$ for $j = 1, 2$, where $z = x + iy$ is a point on the complex plane, and $\psi_j(x, y)$ stands for the stream function in each fluid layer. Following Belward and Forbes [22], we introduce the complex velocity as

$$\chi_j = \begin{cases} \frac{dw_j}{dz} - 1 = \phi_{jx} - i\phi_{jy} - 1, & j = 1, \\ \frac{dw_j}{dz} - \beta = \phi_{jx} - i\phi_{jy} - \beta, & j = 2. \end{cases} \tag{31}$$

The Cauchy integral formula is applied to $\chi_1$ for the lower fluid layer, and a sketch of the integration contour $\mathcal{C}$ is shown in Fig. 3(a). It consists of the interface, channel bottom, and vertical lines joining them at $x = \pm L$ with $L \to \infty$. Since we are interested in the values of $\chi_1$ on the interface and bottom, the Cauchy integral formula gives

$$\begin{aligned} \pi(\Phi_1'X'(s) - 1) = &\int_{-\infty}^{\infty} \frac{[\Phi_1'(\hat\sigma) - X'(\hat\sigma)][Y(\hat\sigma) - Y(s)] + Y'(\hat\sigma)[X(\hat\sigma) - X(s)]}{[X(\hat\sigma) - X(s)]^2 + [Y(\hat\sigma) - Y(s)]^2} d\hat\sigma \\ &- \int_{-\infty}^{\infty} \frac{\{u(\hat\sigma)[1 + b_x(\hat\sigma)^2] - 1\}[b(\hat\sigma) - Y(s)] + b_x(\hat\sigma)[\hat\sigma - X(s)]}{[\hat\sigma - X(s)]^2 + [b(\hat\sigma) - Y(s)]^2} d\hat\sigma, \end{aligned} \tag{32}$$

and

$$\begin{aligned} \pi[u(x) - 1] = &\int_{-\infty}^{\infty} \frac{[\Phi_1'(\hat\sigma) - X'(\hat\sigma)][Y(\hat\sigma) - b(x)] + Y'(\hat\sigma)[X(\hat\sigma) - x]}{[X(\hat\sigma) - x]^2 + [Y(\hat\sigma) - b(x)]^2} d\hat\sigma \\ &- \int_{-\infty}^{\infty} \frac{\{u(\hat\sigma)[1 + b_x(\hat\sigma)^2\} - 1][b(\hat\sigma) - b(x)] + b_x(\hat\sigma)(\hat\sigma - x)}{(\hat\sigma - x)^2 + [b(\hat\sigma) - b(x)]^2} d\hat\sigma, \end{aligned} \tag{33}$$

where $\hat\sigma$ represents the value of the arclength at the varying point on the contour; the evaluation points $s$ and $x$ are placed on the interface and the bottom, respectively; $\Phi_1$ is the velocity potential at the interface; and $u(\hat\sigma)$ stands for the horizontal velocity at the channel bottom.

Next, the Cauchy integral formula is applied to the function $\chi_2$ for the upper fluid layer. A modification to the integration path is modified to avoid setting mesh points on the top wall. Indeed, the impermeability boundary conditions can be satisfied automatically by using the method of

images. Figure 3(b) shows a sketch of the new integration path. Denoting the velocity potential at the interface by $\Phi_2$, the Cauchy integral formula thus leads to

$$\begin{aligned}
&\pi[\Phi_2'(s)X'(s)-\beta]\\
&\quad=\int_{-\infty}^{\infty}\frac{-[\Phi_2'(\hat\sigma)-\beta X'(\hat\sigma)][Y(\hat\sigma)-Y(s)]-\beta Y'(\hat\sigma)[X(\hat\sigma)-X(s)]}{[X(\hat\sigma)-X(s)]^2+[Y(\hat\sigma)-Y(s)]^2}d\hat\sigma\\
&\quad-\int_{-\infty}^{\infty}\frac{-[\Phi_2'(\hat\sigma)-\beta X'(\hat\sigma)][2+2D-Y(\hat\sigma)-Y(s)]-\beta Y'(\hat\sigma)[X(\hat\sigma)-X(s)]}{[X(\hat\sigma)-X(s)]^2+[2+2\Theta-Y(\hat\sigma)-Y(s)]^2}d\hat\sigma. \qquad (34)
\end{aligned}$$

Since we confine our attention to hydraulic falls in the present paper, the solution approaches constant states on both sides in the far field. It is sufficient to perform numerical computations in a truncated domain. We introduce a set of mesh grids equally distributed on the interface, denoted as $s_j$, $j=1,2,\ldots,M$, and the corresponding unknowns

$$\frac{d\Phi_1}{ds}(s_j),\quad \frac{d\Phi_2}{ds}(s_j),\quad \frac{dY}{ds}(s_j).$$

$X'(s_j)$ can be obtained through the parametric equation (29). Similarly, the $N$ mesh points $x_j$, $j=1,2,\ldots,N$, can be defined at the bottom, and $u(x_j)$ are the associated unknowns. To avoid the singularities in computations of the Cauchy integrals, we introduce the other two sets of mesh grids,

$$\begin{aligned}
s_j^m&=\frac{s_j+s_{j+1}}{2},\quad j=1,2,\ldots,M-1,\\
x_j^m&=\frac{x_j+x_{j+1}}{2},\quad j=1,2,\ldots,N-1.
\end{aligned}$$

Evaluating Eqs. (32)–(34) at the midpoints results in $2M+N-3$ algebraic equations, and the dynamic boundary condition at the interface (30) provides additional $M$ equations while being evaluated at the mesh points $\{s_j\}$. We can determine $\beta_1$ by enforcing $\beta_1=\frac{1}{Y(s_M)}$ to satisfy the downstream far-field condition. We can further obtain $\beta_2$ based on conservation of the total fluid height in the far-field, namely solving for $\beta_2$ from

$$1+\Theta=\frac{1}{\beta_1}+\frac{\Theta}{\beta_2}. \qquad (35)$$

Then, substituting the downstream far-field state into the dynamic boundary condition yields

$$\frac{1}{2}F_{1u}^2R\beta^2\left(1-\beta_2^2\right)+\frac{1}{2}F_{1u}^2\left(\beta_1^2-1\right)+(1-R)\left(\frac{1}{\beta_1}-1\right)=0, \qquad (36)$$

which gives the value of $F_{1u}$. Finally, to solve the system by Newton iterations, three more equations describing the flow in the far-field are needed to close the system. These equations can be defined depending on the form of solution to be found; for example, $Y'(1)=0$, $u(1)=1$, and $\Phi_2'(1)=\beta$ (see Refs. [1,16] for details). This numerical scheme was successfully implemented by Refs. [1,6,9,10] for computing free-surface hydraulic falls and Refs. [16,22] for interfacial waves over a single obstacle.

### B. Results

Following Refs. [1,9,10], the numerical computations are performed by assuming that the bottom topography features a combination of separated half-period cosine-type profiles, namely

$$b(x)=\begin{cases}A_1\cos^2\left[\frac{\pi(x-x_1)}{L_1}\right], & \text{for } -\frac{L_1}{2}<x-x_1<\frac{L_1}{2},\\ A_2\cos^2\left[\frac{\pi(x-x_2)}{L_2}\right], & \text{for } -\frac{L_2}{2}<x-x_2<\frac{L_2}{2},\\ 0, & \text{for } |x-x_1|>\frac{L_1}{2},\quad |x-x_2|>\frac{L_2}{2},\end{cases} \qquad (37)$$

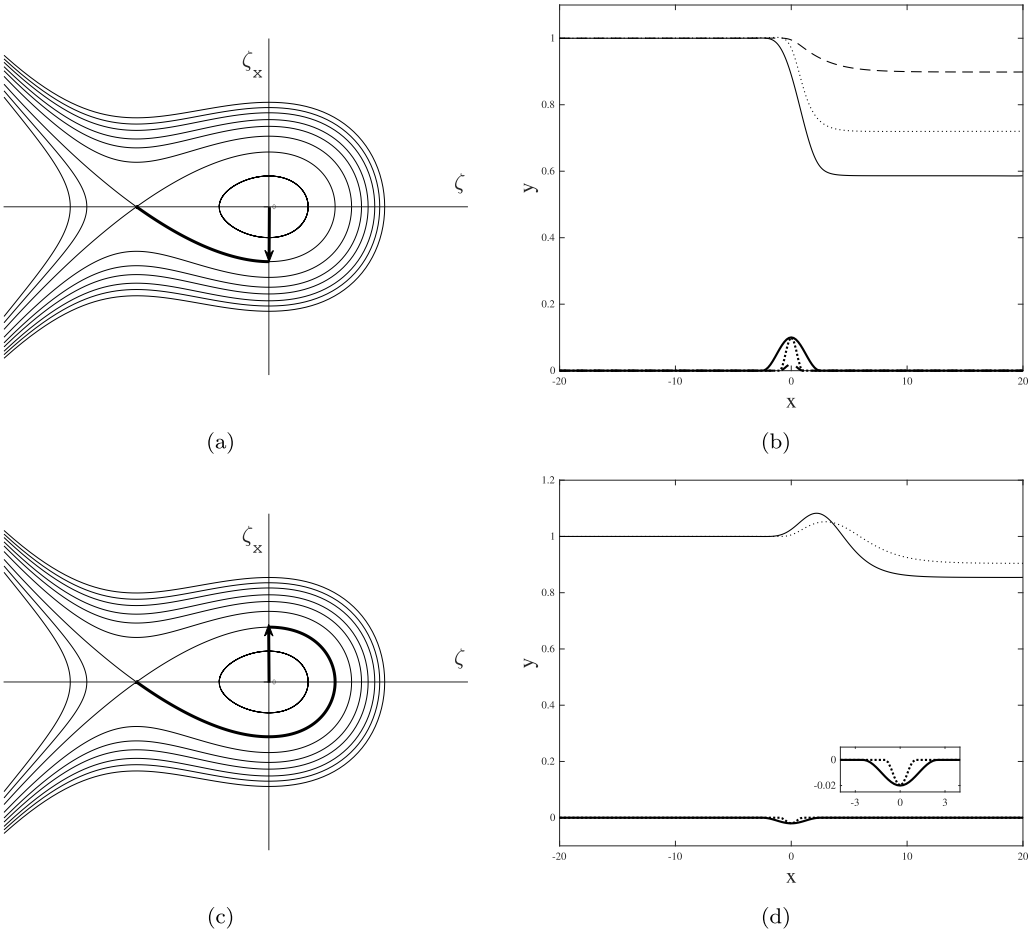


FIG. 4. Interfacial hydraulic falls over one obstacle in Regime (I). (a) Phase portrait for the KdV equation with the topography approximated by a positive Dirac $\delta$ function. (b) Wave profiles of the full Euler equations for convex obstacles with different sizes: $A_1 = 0.1$, $L_1 = 5$, $F_{1u} = 0.4$ (solid line); $A_1 = 0.1$, $L_1 = 2$, $F_{1u} = 0.46$ (dotted line); $A_1 = 0.02$, $L_1 = 2$, $F_{1u} = 0.52$ (dashed line). (c) Phase portrait for the KdV equation with the topography approximated by a negative Dirac $\delta$ function. (d) Wave profiles of the full Euler equations for concave obstacles with different widths: $A_1 = -0.02$, $L_1 = 5$, $F_{1u} = 0.51$ (solid line); $A_1 = -0.02$, $L_1 = 2$, $F_{1u} = 0.53$ (dotted line).

where $A_j$ and $L_j$ are the height and width of obstacles, respectively, and two obstacles are centered at $x = x_1$ and $x = x_2$. The height of the obstacle may be positive, negative, or zero, but two heights cannot be zero simultaneously.

### *1. Single obstacle*

Hydraulic falls of a two-layer flow over a single obstacle are numerically calculated and compared to the theoretical results predicted by the forced KdV equation. In this section, $A_2$ is chosen to be zero so that only one obstacle exists at the bottom. The parameter $R = 0.6$ is fixed and we select $\Theta = 2$ for the case of the thick upper layer and $\Theta = 0.5$ for the case of the thick lower layer, and accordingly, the critical Froude numbers are $F_{1u}^* = 0.55$ and $F_{1u}^* = 0.43$, respectively. The initial guess for Newton's iteration is essential in our computations. To overcome this difficulty, solutions to the associated KdV equation that provide qualitative approximations to the full Euler equations,

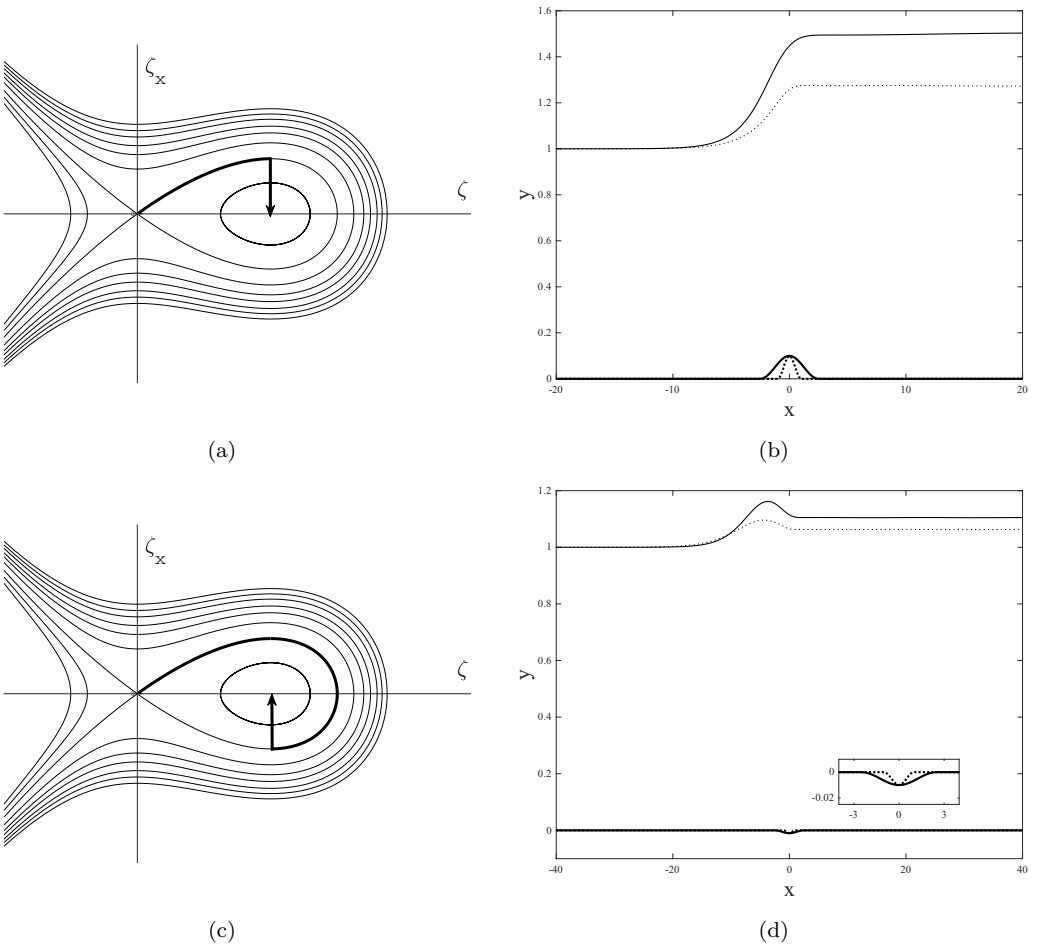


FIG. 5. Interfacial hydraulic falls over one obstacle in Regime (II). (a) Phase portrait for the KdV equation with the topography approximated by a positive Dirac $\delta$ function. (b) Wave profiles of the full Euler equations for convex obstacles with different widths: $A_1 = 0.1$, $L_1 = 5$, $F_{1u} = 0.63$ (solid line); $A_1 = 0.1$, $L_1 = 2$, $F_{1u} = 0.61$ (dotted line). (c) Phase portrait for the KdV equation with the topography approximated by a negative Dirac $\delta$ function. (d) Wave profiles of the full Euler equations for concave obstacles with different widths: $A_1 = -0.02$, $L_1 = 5$, $F_{1u} = 0.58$ (solid line); $A_1 = -0.02$, $L_1 = 2$, $F_{1u} = 0.57$ (dotted line).

are analyzed before performing direct numerical simulations. For example, the parameter $\beta_1$ is chosen to be greater than one if the weakly nonlinear theory predicts that the depth downstream is smaller than upstream. Interfacial hydraulic falls resulting from various heights and widths of the obstacle will be investigated to illustrate the effects of the spatial scale characteristics of the obstruction.

We first consider Regime (I): subcritical flow upstream with a thick upper layer. Figure 4(a) shows the phase portrait of the homogeneous KdV equation plotted using the system (26) with the negative nonlinear term and $\lambda < 0$. When the equation is forced by a topography described as a positive Dirac $\delta$ function, since the flow is uniform upstream with $\zeta = 0$, the solution must jump downwards to satisfy the jump condition (25) and then move along the trajectory to the saddle point. Thus, a hydraulic fall is obtained. Figure 4(b) demonstrates that interfacial hydraulic falls calculated numerically with the full Euler equations are qualitatively similar to the weakly nonlinear theory. Results of various sizes of the obstacle are compared. It is evident in Fig. 4(b) that for a

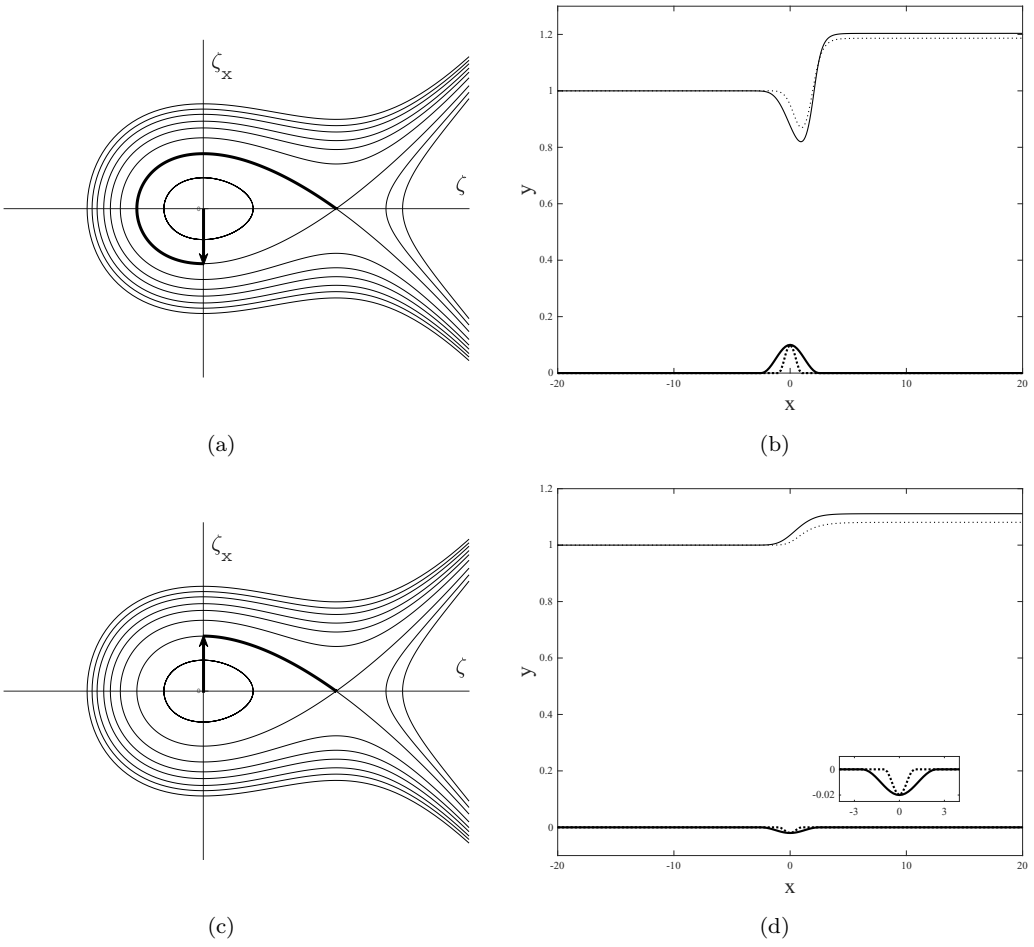


FIG. 6. Interfacial hydraulic falls over one obstacle in Regime (III). (a) Phase portrait for the KdV equation with the topography approximated by a positive Dirac $\delta$ function. (b) Wave profiles of the full Euler equations for convex obstacles with different widths: $A_1 = 0.1, L_1 = 5, F_{1u} = 0.33$ (solid line); $A_1 = 0.1$, $L_1 = 2, F_{1u} = 0.35$ (dotted line). (c) Phase portrait for the KdV equation with the topography approximated by a negative Dirac $\delta$ function. (d) Wave profiles of the full Euler equations for concave obstacles with different widths: $A_1 = -0.02, L_1 = 5, F_{1u} = 0.39$ (solid line); $A_1 = -0.02, L_1 = 2, F_{1u} = 0.40$ (dotted line).

positive, convex obstacle, as the width $L_1$ enlarges, the upstream Froude number $F_{1u}$ decreases, and the vertical drop of the fall (namely $|H_1 - h_1|$) becomes more significant. In addition, increasing the obstacle's height leads to a reduction of $F_{1u}$ and an amplification of $|H_1 - h_1|$. When the obstacle is concave ($Q < 0$), the solution must jump upwards in the weakly nonlinear analysis to satisfy the jump condition. So a nonequilibrium stationary point corresponding to the peak of the solution is passed before reaching the saddle point. In this case, hydraulic falls are expected to rise and fall over the obstacle, with the depth of the lower fluid being smaller downstream than upstream [see Fig. 4(c)]. For concave bottom obstructions, Fig. 4(d) shows the full Euler computations with the solutions featuring a nonmonotonic structure which agrees well with the theoretical prediction. Tendencies similar to Fig. 4(b) are also found when the aspect ratio of the obstruction is changed.

In the same vein, the KdV-based analysis can be carried out for the other three cases (see the phase portraits in Figs. 5–7), and the details will not be repeated hereafter. Interfacial hydraulic falls in Regime (II), supercritical flow upstream with a thick upper layer, show a more significant depth of

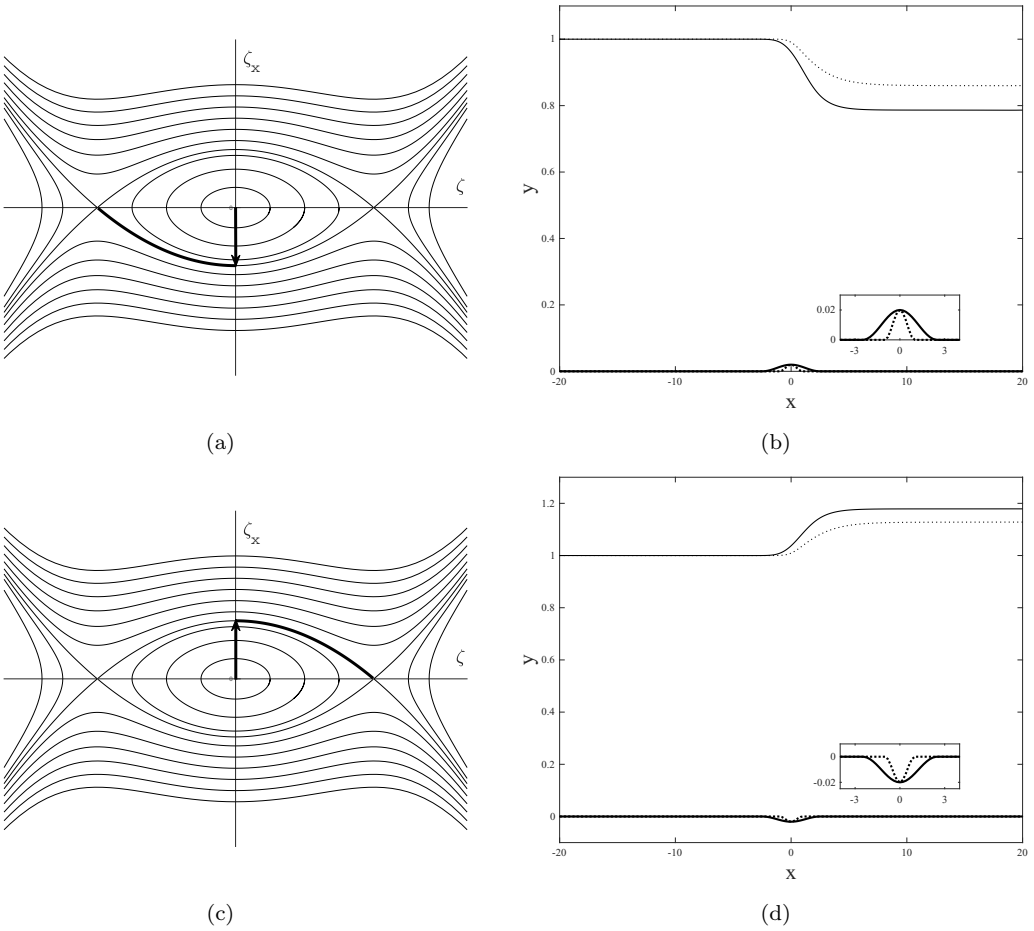


FIG. 7. Interfacial hydraulic falls over one obstacle in Regime (IV) with $\Theta = \sqrt{3/5}$ and $F_{1u}^* = 0.48$. (a) Phase portrait for the KdV equation with the topography approximated by a positive Dirac $\delta$ function. (b) Wave profiles of the full Euler equations for convex obstacles with different widths: $A_1 = 0.02$, $L_1 = 5$, $F_{1u} = 0.45$ (solid line); $A_1 = 0.02$, $L_1 = 2$, $F_{1u} = 0.46$ (dotted line). (c) Phase portrait for the KdV equation with the topography approximated by a negative Dirac $\delta$ function. (d) Wave profiles of the full Euler equations for concave obstacles with different widths: $A_1 = -0.02$, $L_1 = 5$, $F_{1u} = 0.45$ (solid line); $A_1 = -0.02$, $L_1 = 2$, $F_{1u} = 0.46$ (dotted line).

the lower fluid downstream than upstream, meaning that they are "jump-ups." In Figs. 5(b) and 5(d), $F_{1u}$ and $|H_1 - h_1|$ increase with the broadening of the obstacle. For concave obstacles, hydraulic falls feature a bulge structure rather than a monotonic increasing curve. This phenomenon differs slightly from Regime (I) since the lower layer ultimately reaches a higher level as $x \to +\infty$, namely $h_1 > H_1$. The results of Regime (III)—subcritical flow upstream with a thick lower layer—and Regime (IV)—subcritical flow upstream with a critical depth—are presented in Figs. 6 and 7, respectively. Similar behaviors akin to Regime (I), a reduction of $F_{1u}$, and an amplification of $|H_1 - h_1|$ alongside the increase of $L_1$, are observed. It is worth mentioning that the concave obstruction can lead to hydraulic jump-ups in Regime (IV), as seen in Fig. 7(d). That is because the flow upstream has to jump upwards at the equilibrium point ($\zeta = 0$, $\zeta_x = 0$) to satisfy the jump condition (25) and moves to the right saddle point in the phase portrait of the forced mKdV equation [see Fig. 7(c)].

In summary, broadening the obstacle increases the vertical jump of the interfacial hydraulic fall. At the same time, it decreases the Froude number upstream for subcritical flows and increases the

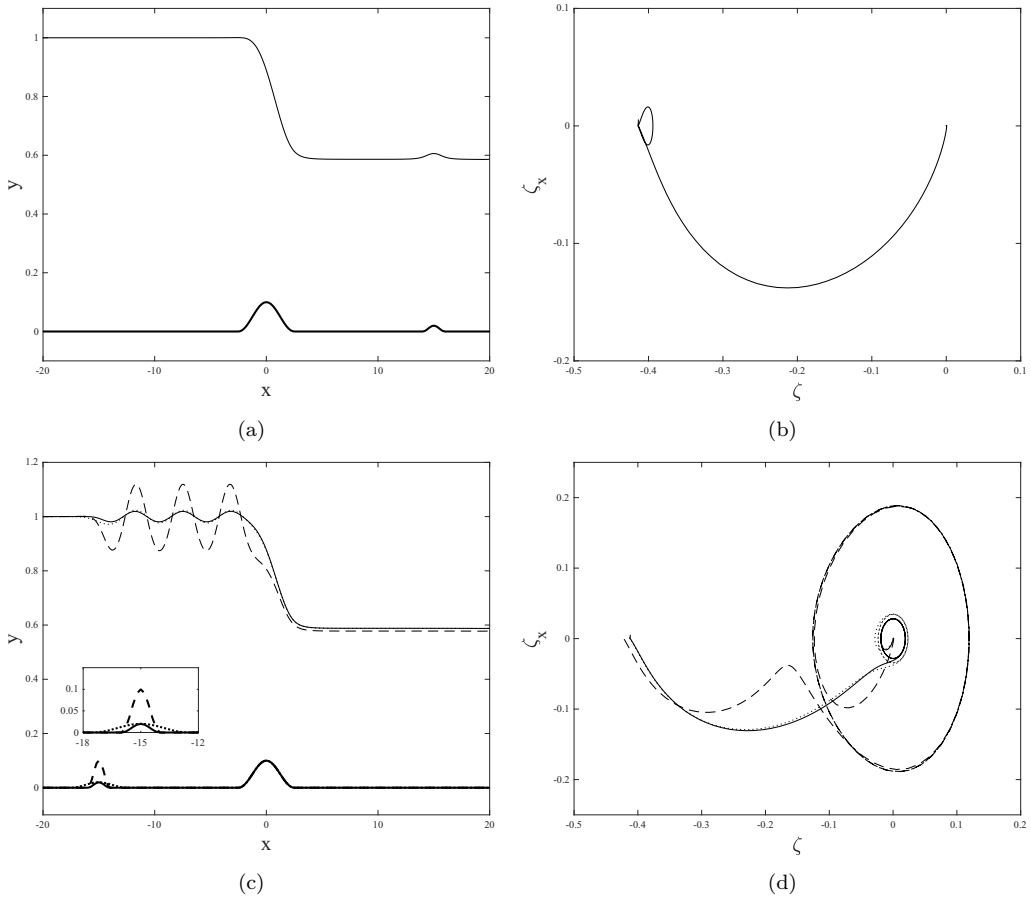


FIG. 8. Interfacial hydraulic falls over two convex obstacles in Regime (I) with $A_1 = 0.1$, $L_1 = 5$, and $x_1 = 0$. [(a) and (b)] A soliton-like solution and its phase portrait in the full Euler equations with $A_2 = 0.02$, $L_2 = 2$, and $x_2 = 15$. [(c) and (d)] Trapped wave solutions and their phase portraits for $x_2 = -15$ and various aspect ratios of the second obstacle: $A_2 = 0.02$, $L_2 = 2$, $\lambda_c \approx 4.3$ (solid line); $A_2 = 0.02$, $L_2 = 5$, $\lambda_c \approx 4.3$ (dotted line); $A_2 = 0.1$, $L_2 = 2$, $\lambda_c \approx 4.2$ (dashed line).

Froude number upstream for supercritical flows. The numerical solutions are coherent with the phase portraits based on the KdV or mKdV equation, partially validating our numerical algorithms. The solutions obtained in this subsection provide good initial data for the Newton iteration when computing trapped waves between two successive obstacles in the next subsection.

### *2. Two successive obstacles*

We extend the problem to a two-layer flow past two successive obstacles, one of which is placed at the origin, and the other can be placed upstream or downstream. The main focus of this part is on the existence and wavelength of trapped waves. The influences of horizontal and vertical sizes of the obstacles and their relative distance are considered. We find that the solutions are very sensitive to the initial conditions we choose. For our code to converge quickly, the hydraulic fall solutions over a single obstacle computed in the precedent subsection are used as the initial data for the Newton iteration. And the second obstacle can be introduced using a numerical homotopy continuation by increasing its amplitude gradually until the desired value. The wavelengths of trapped waves can be predicted theoretically with the dispersion relation given in Eqs. (11) and (13), and the

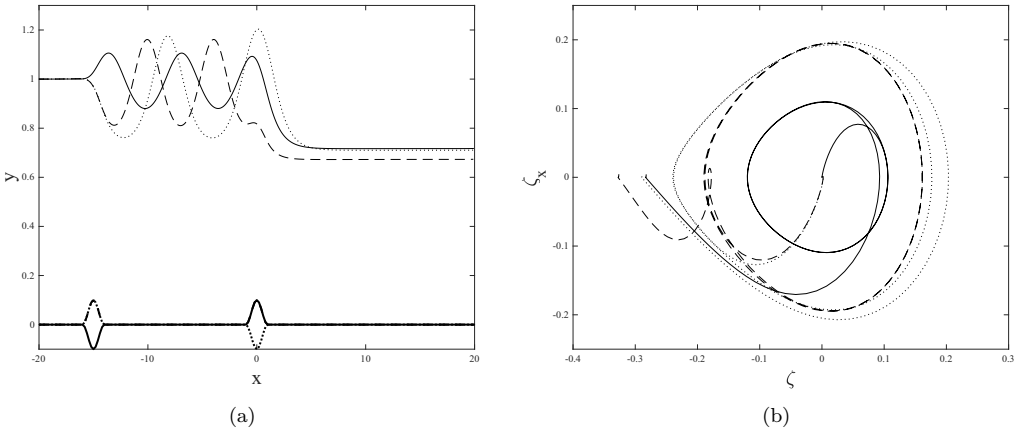


(a) (b)

FIG. 9. Interfacial hydraulic falls over two successive obstacles of mixed type in Regime (I). The wave profiles (a) and phase portraits (b) are obtained by solving the full Euler equations with $L_1 = L_2 = 2$, $x_1 = 0$, and $x_2 = -15$; other parameters are $A_1 = 0.1$, $A_2 = -0.1$, $\lambda_c \approx 6.6$ (solid line); $A_1 = -0.1$, $A_2 = 0.1$, $\lambda_c \approx 8.1$ (dotted line). The numerical results with two successive convex obstacles are presented for comparison and the parameters are $A_1 = 0.1$, $A_2 = 0.1$, $\lambda_c \approx 6.2$ (dashed line).

predictions are compared with the numerical results of the full Euler equations. It is noted that the theoretical wavelength is obtained using the upstream/downstream Froude number arising from the case with a single obstruction fixed at the origin (while the second obstruction is just considered an additional disturbance). This approximation will be shown to provide satisfactory agreement with the computed result in subsequent analyses. The parameters $\Theta$ and $R$ remain the same as the previous subsection for four different regimes.

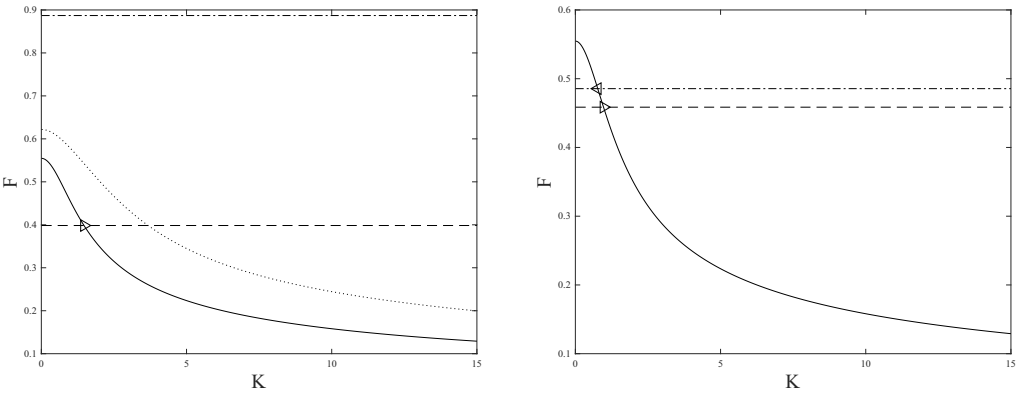


(a) (b)

FIG. 10. Dispersion relations, $F_{1u}$ (solid lines) and $F_{1d}$ (dotted line) given in Eqs. (11) and (13) with $(\Theta, R, \beta) = (2, 0.6, 1)$, and predicted wave numbers for Regime (I). (a) The theoretical prediction of the wave number for the cases in Fig. 8(c). The obtained upstream Froude number (horizontal dashed line) and downstream Froude number (horizontal dash-dotted line) indicate trapped waves upstream with $\lambda_t \approx 4.3$ (triangle). (b) For the cases in Fig. 9, the computed upstream Froude numbers (horizontal dashed and dash-dotted lines) intersecting the dispersion relation (11) gives the theoretical wave numbers of trapped waves: $\lambda_t \approx 6.5$ for $(A_1, A_2) = (0.1, -0.1)$ and $\lambda_t \approx 8.2$ for $(A_1, A_2) = (-0.1, 0.1)$.

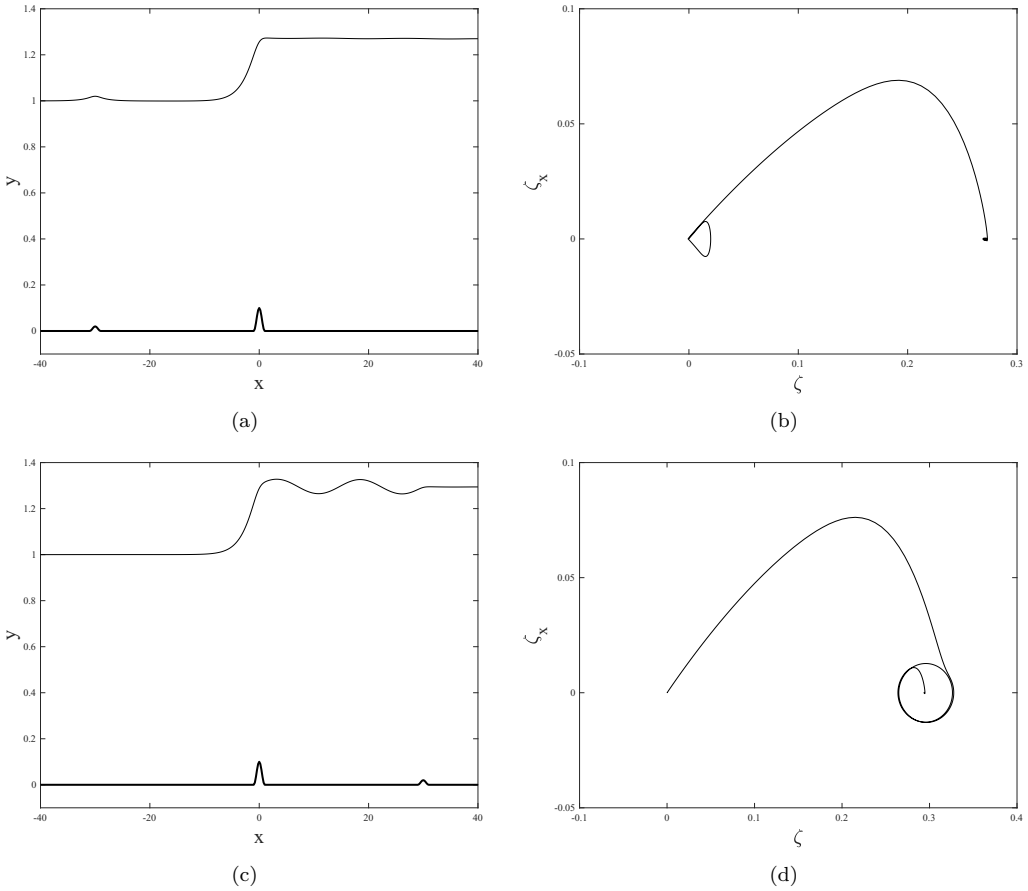


FIG. 11. Interfacial hydraulic falls over two successive convex obstacles in Regime (II), computed in the full Euler equations with $(A_1, L_1, x_1) = (0.1, 2, 0)$ and $(A_2, L_2, x_2) = (0.02, 2, \pm 30)$. [(a) and (b)] Wave profile and phase portrait for $x_2 = -30$. [(c) and (d)] Wave profile and phase portrait for $x_2 = 30$, exhibiting trapped waves downstream with $\lambda_c \approx 15.2$.

When the flows upstream are in Regime (I), interfacial hydraulic falls over two successive convex obstacles are numerically computed, with fixed geometrical parameters ($A_1 = 0.1$, $L_1 = 5$, and $x_1 = 0$) for one obstacle and variable sizes and locations for the other. Since the upstream flow is subcritical, the linear theory predicts that the second obstacle must be placed upstream of the hydraulic fall to obtain trapped waves, confirmed by the numerical experiments of the full Euler equations shown in Fig. 8. Indeed, when the second obstacle is placed downstream, there are no trapped waves between the two. The interface features a soliton-like form right above the second obstacle [see Fig. 8(a)], akin to the phenomenon occurring in free-surface hydraulic falls described in Ref. [1]. A train of trapped waves appears upstream when the second obstacle is placed upstream [see Fig. 8(c)]. It is observed that a variation in the horizontal or vertical size of the second obstacle only results in the change of amplitude of the trapped waves but does not influence the wavelength significantly. It is not surprising that the higher the second obstacle is, the larger the trapped waves' amplitude; however, the width of the second obstacle has little impact on wave amplitude.

Furthermore, cases for two obstacles having different polarities are calculated with $A_1 = \pm 0.1$ and $A_2 = \mp 0.1$ (see Fig. 9). The numerical result for $A_1 = A_2 = 0.1$ is also presented in the same figure for comparison purposes. It is shown that for a convex obstacle at the origin, changing the

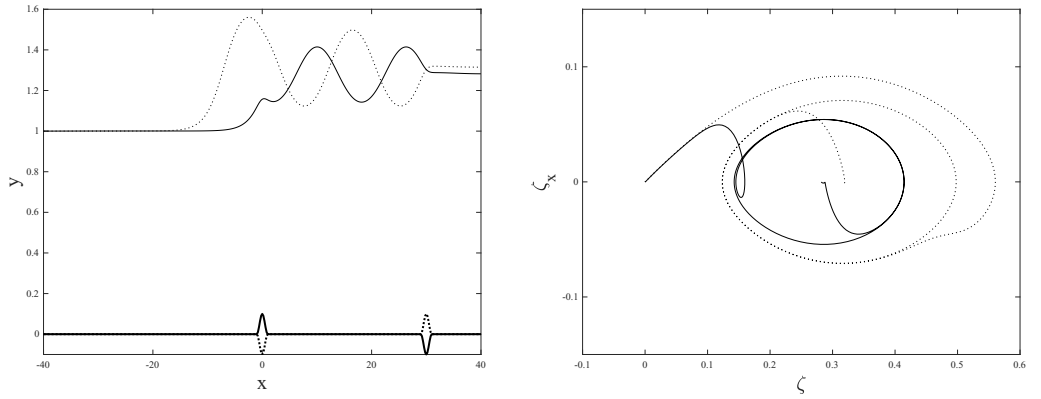


(a) (b)

FIG. 12. Trapped wave profiles (a) and phase portraits (b) of interfacial hydraulic falls over two successive obstacles of mixed type in Regime (II). Solid lines: $(A_1, L_1, x_1) = (0.1, 2, 0)$, $(A_2, L_2, x_2) = (-0.1, 2, 30)$, and $\lambda_c \approx 15.8$; dotted lines: $(A_1, L_1, x_1) = (-0.1, 2, 0)$, $(A_2, L_2, x_2) = (0.1, 2, 30)$, and $\lambda_c \approx 17.3$.

polarity of the second obstacle results in a similar wavelength of the generated trapped waves, but not vice versa, indicating that the wavelength of the trapped waves upstream under this situation depends primarily on the obstacle at the origin. However, the phase portraits in Fig. 9(b) show that the polarity of the second obstruction determines the sign of $\zeta_x$ when leaving the equilibrium point $(\zeta, \zeta_x) = (0, 0)$.

The dispersion relations in Eqs. (11) and (13) are presented in Fig. 10. The theoretical wavelength of upstream trapped waves can be estimated via solving for $K$ in Eq. (11) based on the computed upstream Froude number $F_{1u}$ for the case with single obstruction placed at the origin, namely the

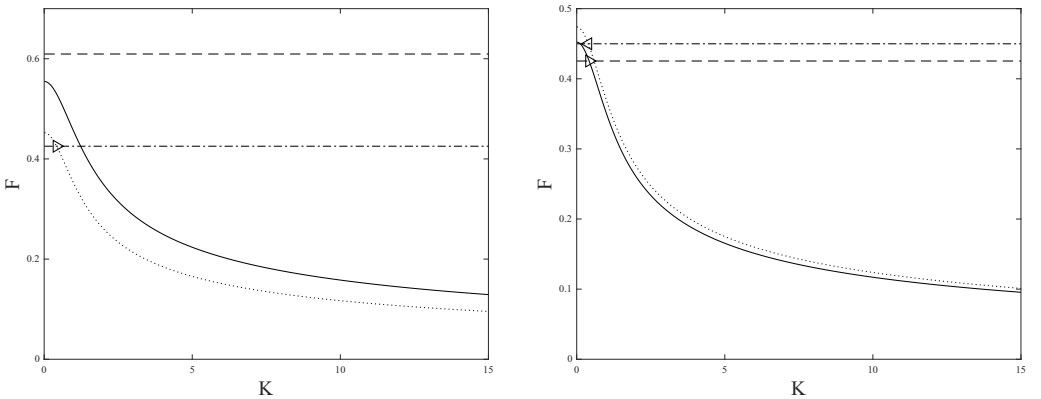


(a) (b)

FIG. 13. Dispersion relations with $(\Theta, R, \beta) = (2, 0.6, 1)$ and predicted wave numbers for Regime (II). (a) Theoretical result ($\lambda_t \approx 15.0$) for the case of Fig. 11(c): dispersion curve $F_{1u}(K)$ (solid line), dispersive curve $F_{1d}(K)$ (dotted line), computed upstream Froude number (horizontal dashed line), and computed downstream Froude number (horizontal dash-dotted line). (b) Theoretical result ($\lambda_t \approx 15.0$) for the solid-line case of Fig. 12: dispersion curve $F_{1d}(K)$ (solid line) and computed downstream Froude number (horizontal dashed line); theoretical result ($\lambda_t \approx 16.1$) for the dotted-line case of Fig. 12: dispersion curve $F_{1d}(K)$ (dotted line) and computed downstream Froude number (horizontal dash-dotted line).

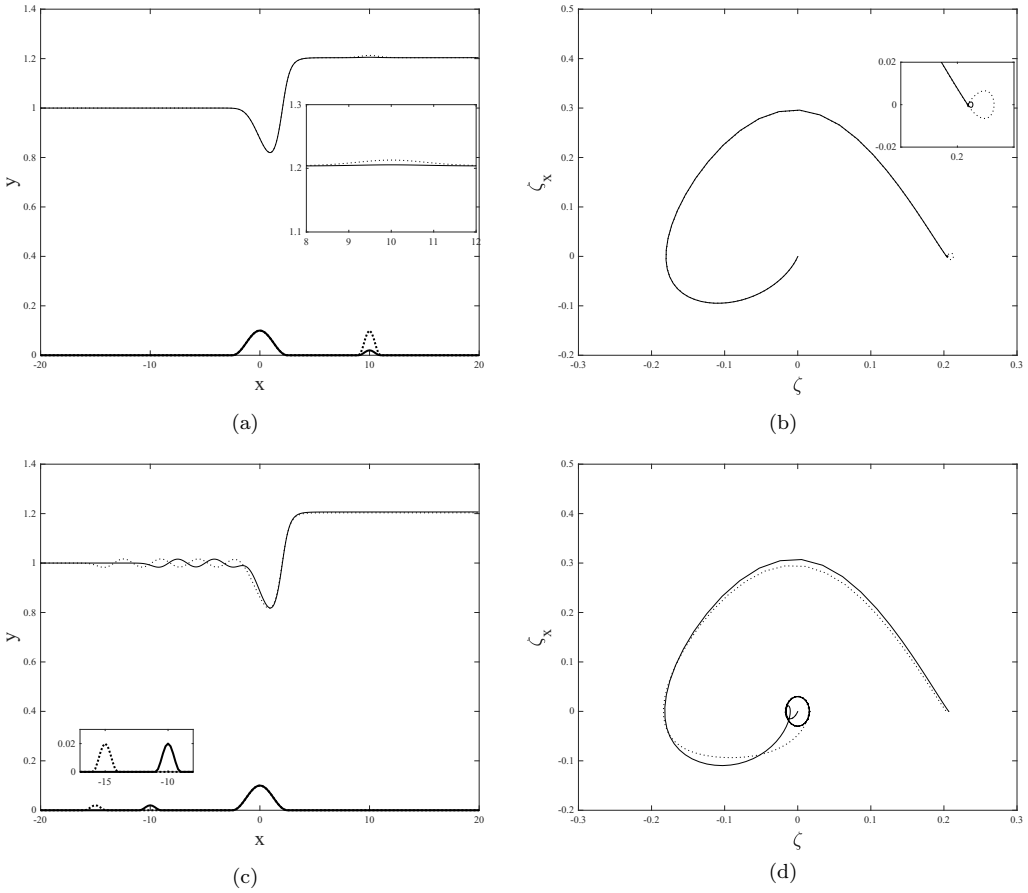


FIG. 14. Wave profiles of interfacial hydraulic falls over two successive convex obstructions and phase portraits in Regime (III), computed with the full Euler equations with $(A_1, L_1, x_1) = (0.1, 5, 0)$ and $L_2 = 2$. Other parameter are [(a) and (b)] $A_2 = 0.02$, $x_2 = 10$ (solid line) and $A_2 = 0.1$, $x_2 = 10$ (dotted line); [(c) and (d)] $A_2 = 0.02$, $x_2 = -10$, $\lambda_c \approx 3.3$ (solid line) and $A_2 = 0.02$, $x_2 = -15$, $\lambda_c \approx 3.4$ (dotted line).

intersection point of $F = F_{1u}$ and the dispersion relation $F = F_{1u}(K)$. Similarly, the intersection point of the horizontal line $F = F_{1d}$ and the dispersion curve $F = F_{1d}(K)$ given in Eq. (13) is used if a train of trapped waves exits downstream. We denote by $\lambda_t$ the theoretical prediction of the wavelength from the linear perspective and by $\lambda_c$ the computed wavelength in the full Euler equations. It is shown in Fig. 10(a) that the upstream Froude number intersecting the upstream linear dispersion relation results in $\lambda_t \approx 4.3$, which offers good agreement with the numerical results shown in Fig. 8(c) and 8(d). Similarly, $\lambda_t \approx 6.5$ and $\lambda_t \approx 8.2$ are predicted [see Fig. 10(b)] for the cases presented in Fig. 9. Note that for hydraulic falls in Regime (I), the downstream Froude numbers are larger than the critical value, meaning that the downstream Froude number cannot intersect with the downstream dispersion relation, which explains why no periodic wave train appears downstream.

Similar numerical experiments are carried out for the other three regimes of upstream flow. The results of hydraulic falls over two successive convex obstacles when the upstream flows are in Regime (II) are presented in Fig. 11. The geometrical parameters of the obstacle at the origin are fixed as $A_1 = 0.1$ and $L_1 = 2$. Since Regime (II) demands supercritical upstream flows, it is impossible to have an intersection point between the upstream Froude number $F = F_{1u}$ and the

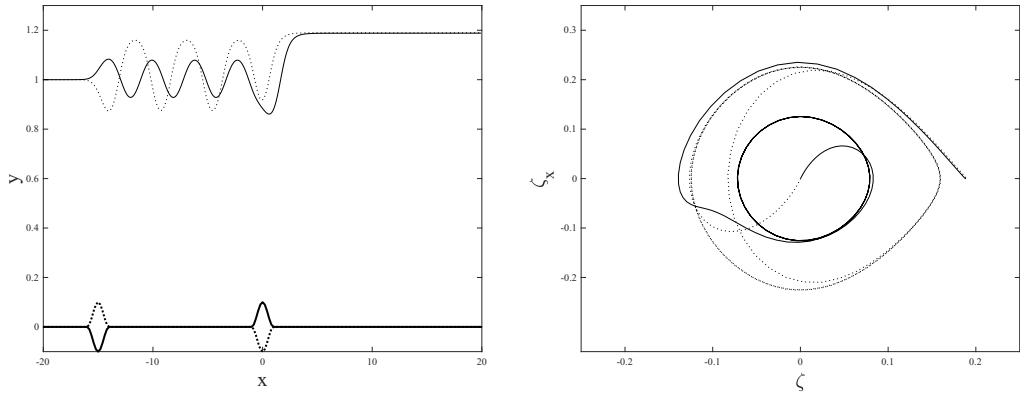


(a) (b)

FIG. 15. Trapped wave profiles (a) and phase portraits (b) of interfacial hydraulic falls over two successive obstacles of mixed type in Regime (III). Solid lines: $(A_1, L_1, x_1) = (0.1, 2, 0)$, $(A_2, L_2, x_2) = (-0.1, 2, -15)$, and $\lambda_c \approx 4.0$; dotted lines: $(A_1, L_1, x_1) = (-0.1, 2, 0)$, $(A_2, L_2, x_2) = (0.1, 2, -15)$, and $\lambda_c \approx 4.7$.

upstream dispersion curve $F = F_{1u}(K)$ [see the solid curve and horizontal dashed line in Fig. 13(a)], indicating that trapped waves can only appear downstream. A typical trapped wave solution is shown in Fig. 11(c). These waves feature a greater wavelength than those in Regime (I), so a more extended computational domain is required. Numerical examples when bottom obstacles are of opposite phases are demonstrated in Fig. 12. To estimate the wavelength of trapped waves, we place the second obstruction further downstream from the origin, say, $x_2 = 30$, in Figs. 11 and 12. For $A_1 = 0.1$ fixed, as shown by the solid lines in Figs. 11(c) and 12(a), the generated

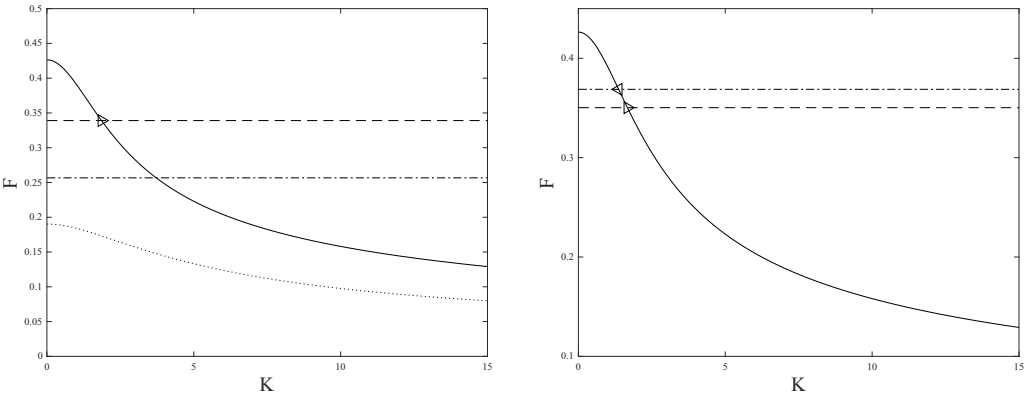


(a) (b)

FIG. 16. Dispersion relations with $(\Theta, R, \beta) = (0.5, 0.6, 1)$ and predicted wave numbers for Regime (III). (a) Theoretical result ($\lambda_t \approx 3.4$) for the cases in Fig. 14(c): Dispersion curve $F_{1u}(K)$ (solid line), dispersion curve $F_{1d}(K)$ (dotted line), computed upstream Froude number (horizontal dashed line), and computed downstream Froude number (horizontal dash-dotted line). (b) Theoretical predictions of wave number for the examples shown in Fig. 15: $\lambda_t \approx 3.8$ for the case $A_1 = 0.1$ and $\lambda_t \approx 5.0$ for the case $A_1 = -0.1$. Solid line: Dispersion curve $F_{1u}(K)$; horizontal dashed line: computed upstream Froude number for the case $A_1 = 0.1$; horizontal dash-dotted line: computed upstream Froude number for the case $A_1 = -0.1$.

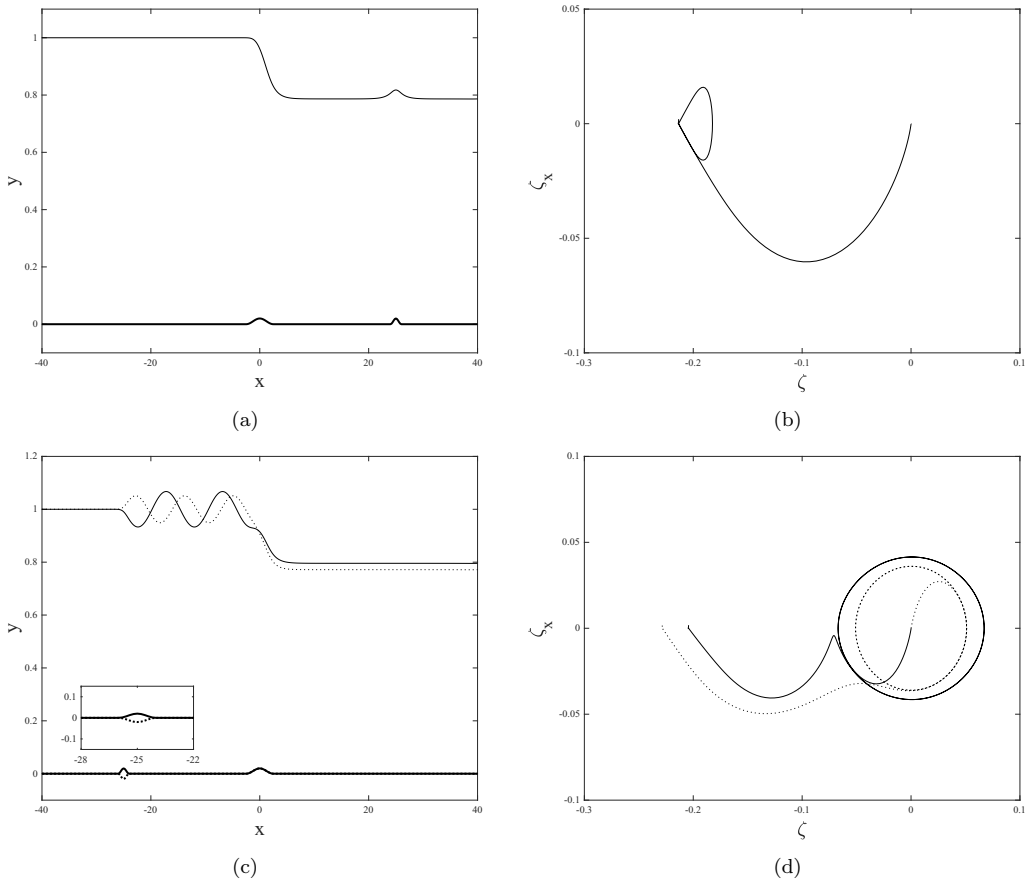


FIG. 17. Wave profiles of interfacial hydraulic falls over two successive obstructions and phase portraits in Regime (IV), computed with the full Euler equations with $(A_1, L_1, x_1) = (0.02, 5, 0)$. Other parameter are [(a) and (b)] $(A_2, L_2, x_2) = (0.02, 2, 25)$; [(c) and (d)] $(A_2, L_2, x_2) = (0.02, 2, -25)$, $\lambda_c \approx 10.4$ (solid line) and $(A_2, L_2, x_2) = (-0.02, 2, -25)$, $\lambda_c \approx 9.1$ (dotted line).

trapped waves have similar wavelengths regardless of the sign and size of $A_2$. This fact implies that changing the phase of the obstacle closer to the subcritical flow does not exert a noticeable influence on the wavelength. The theoretical predictions of wavelength calculated using the linear theory are $\lambda_t \approx 15.0$ for the case in Fig. 11(c) and $\lambda_t \approx 15.0, 16.1$ for the cases in Fig. 12, which show acceptable agreement with the numerical results of the primitive equations. From Figs. 11(c) and 12(a), we can remark that for a fixed $L_2$, a larger size of the second obstacle results in larger amplitude trapped waves, and reversing the phases of the two obstacles have a considerable impact on the amplitude and wavelength of trapped waves.

Numerical results for upstream flows in Regime (III) are presented in Figs. 14 and 15. According to the dispersion relations shown in Fig. 16, trapped waves only appear upstream. The effect of the size of the second obstacle placed downstream can be observed from Figs. 14(a) and 14(b): Increasing the height of the second obstacle leads to a slight rise in amplitude of the soliton-like wave right above it. The effect of the distance between two obstacles on trapped waves is shown in Figs. 14(c) and 14(d). It is found that the variation of the distance between the obstacles only influences the number of waves trapped between the two but has little impact on the wavelength and amplitude of the waves. This is comparable with the results of the single-layer case; see Vanden-Broeck and Dias [1] for the fully nonlinear solutions and Pratt [24] for experimental results.

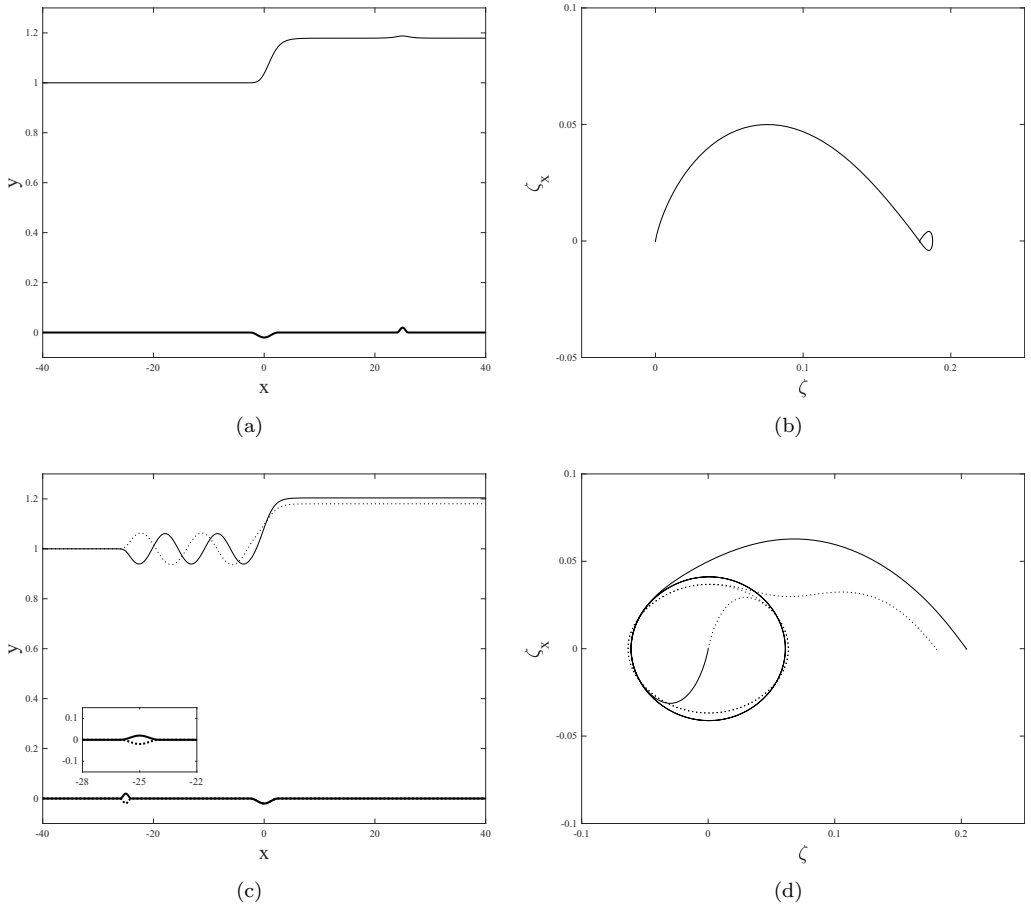


FIG. 18. Wave profiles of interfacial hydraulic falls over two successive obstructions and phase portraits in Regime (IV), computed with the full Euler equations with $(A_1, L_1, x_1) = (-0.02, 5, 0)$. Other parameter are [(a) and (b)] $(A_2, L_2, x_2) = (0.02, 2, 25)$; [(c) and (d)] $(A_2, L_2, x_2) = (0.02, 2, -25)$, $\lambda_c \approx 9.5$ (solid line) and $(A_2, L_2, x_2) = (-0.02, 2, -25)$, $\lambda_c \approx 11.0$ (dotted line).

Similarly to Regime (I) associated with subcritical flows upstream, the predictions of wavelength are made by using the intersection point between the upstream Froude number and the upstream dispersion relation. The corresponding results, $\lambda_t \approx 3.4$ for the cases in Figs. 14(c) and 14(d) and $\lambda_t \approx 3.8$, 5.0 for the cases in Fig. 15, agree well with the numerical solutions.

Figures 17 and 18 show the numerical results for Regime (IV), namely subcritical flow upstream with critical depth past two successive obstacles. Similarly to Regimes (I) and (III), trapped waves in Regime (IV) only exist upstream [see Figs. 17(c) and 18(c)]. The train of waves is predicted by the linear dispersion relation shown in Fig. 19(a) when a convex obstruction is located at the origin [see also Fig. 19(b) for the case with a concave obstruction]. The wavelength of the trapped waves is in rough agreement with that indicated by the linear theory. In this case, the difference between wavelengths of trapped waves computed with different phases of the second obstacle cannot be ignored [see Figs. 17(c) and 18(c)], implying that the second obstacle may play a role when its amplitude becomes comparable with the one at the origin.

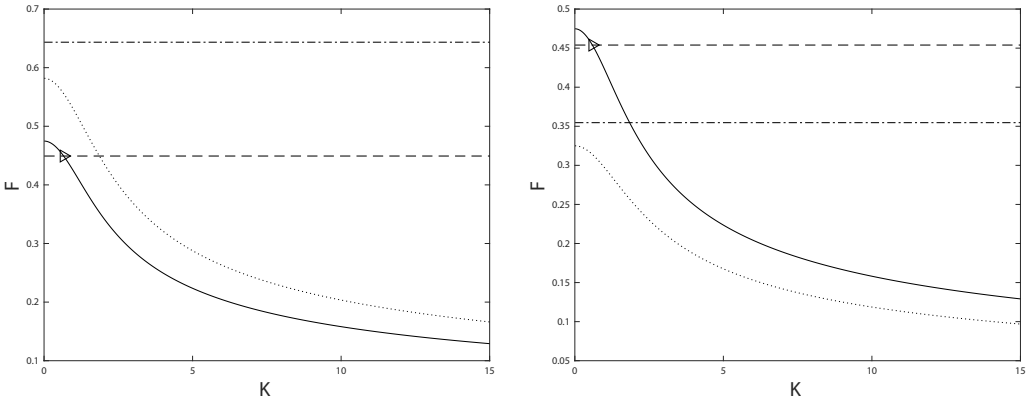


FIG. 19. Dispersion relation with $(\Theta, R, \beta) = (0.77, 0.6, 1)$ and predicted wave numbers for Regime (IV). (a) Theoretical result ($\lambda_t \approx 9.5$) for the cases in Fig. 17(c): Dispersion curve $F_{1u}(K)$ (solid line), dispersion curve $F_{1d}(K)$ (dotted line), computed upstream Froude number (horizontal dashed line), and computed downstream Froude number (horizontal dash-dotted line). (b) Theoretical result ($\lambda_t \approx 10.6$) for the cases in Fig. 18(c): Dispersion curve $F_{1u}(K)$ (solid line), dispersion curve $F_{1d}(K)$ (dotted line), computed upstream Froude number (horizontal dashed line), and computed downstream Froude number (horizontal dash-dotted line).

## V. CONCLUSIONS

Most existing studies on hydraulic falls for a steady flow past localized bottom topography focus on one-layer flow past one obstacle or two successive obstacles and two-layer flow past a single obstruction. We have extended the configuration to a two-layer flow past two successive obstacles in the present paper. We first followed the conventional wisdom to derive the weakly nonlinear theory (the KdV type equations with the bottom topography served as the external forcing) to understand the mechanisms of existence and classification of hydraulic fall solutions. Interfacial hydraulic fall solutions over a single obstacle can be divided into six categories according to flow properties upstream, four of which have been carefully studied in the paper: subcritical flow upstream with a thick upper layer, supercritical flow upstream with a thick upper layer, subcritical flow upstream with a thick bottom layer, and subcritical flow upstream with critical depth. The phase portrait analyses of the KdV type equations with the force of the $\delta$-function form indicate that the convexity-concavity property of the obstacle can lead to different interface profiles. This statement has been confirmed by the numerical computations of the full Euler equations based on a boundary integral equation method. It has also been shown numerically that increasing the vertical or horizontal size of the obstacle increases the vertical drop of the fall.

When the second obstacle is added to the system, the existence of trapped waves depends on its position. Numerical computations of the fully nonlinear equations show that the second obstruction has to be placed on the subcritical side of the fall to generate trapped waves. Varying the horizontal or vertical size of the second obstacle or its relative distance to the first obstacle exerts little influence on the wavelength of the generated trapped waves though the amplitude may change significantly. However, changing the phase of the first obstacle from convex to concave can considerably affect the wavelength. The wavelength of trapped waves can also be estimated based on the linear theory by intersecting the computed subcritical Froude number with the linear dispersion curve. The prediction can be accurate enough with less than a few percent relative error.

When the upstream flow is supercritical, the numerics for the full Euler equations seem more challenging. We did not manage to find solutions in the remaining two regimes: supercritical flow upstream with a thick bottom layer and supercritical flow upstream with critical depth. These two

cases are also interesting and merit further investigation. Additionally, recent work on modeling and field observations of hydraulic fall for three-layer flow past a bottom obstacle (see Chesnokov [25], for example) also stimulates us to find steady solutions in the same configuration.

**ACKNOWLEDGMENT**

This work was supported by the National Natural Science Foundation of China (Grants No. 11911530171 and No. 11772341), the key program of the National Natural Science Foundation of China (Grant No. 12132018), and the Royal Society International Exchanges Travel Grant (No. IEC/NSFC/181279).

[1] F. Dias and J.-M. Vanden-Broeck, Trapped waves between submerged obstacles, J. Fluid Mech. **509**, 93 (2004).
[2] L. K. Forbes and L. W. Schwartz, Free-surface flow over a semicircular obstruction, J. Fluid Mech. **114**, 299 (1982).
[3] J.-M. Vanden-Broeck, Free-surface flow over an obstruction in a channel, Phys. Fluids **30**, 2315 (1987).
[4] L. K. Forbes, Critical free-surface flow over a semi-circular obstruction, J. Eng. Math. **22**, 3 (1988).
[5] F. Dias and J.-M. Vanden-Broeck, Open channel flows with submerged obstructions, J. Fluid Mech. **206**, 155 (1989).
[6] F. Dias and J.-M. Vanden-Broeck, Generalised critical free-surface flows, J. Eng. Math. **42**, 291 (2002).
[7] B. J. Binder, J.-M. Vanden-Broeck, and F. Dias, Forced solitary waves and fronts past submerged obstacles, Chaos **15**, 037106 (2005).
[8] C. Page and E. I. Părău, Time dependent hydraulic falls and trapped waves over submerged obstructions, Phys. Fluids **26**, 126604 (2014).
[9] C. Page, S. Grandison, and E. I. Părău, The influence of surface tension upon trapped waves and hydraulic falls, Eur. J. Mech. B Fluids **43**, 191 (2014).
[10] C. Page and E. I. Părău, Hydraulic falls under a floating ice plate due to submerged obstructions, J. Fluid Mech. **745**, 208 (2014).
[11] D. Farmer and L. Armi, Stratified flow over topography: the role of small-scale entrainment and mixing in flow establishment, Proc. R. Soc. Lond. A **455**, 3221 (1999).
[12] L. K. Forbes, Two-layer critical flow over a semi-circular obstruction, J. Eng. Math. **23**, 325 (1989).
[13] H. Sha and J.-M. Vanden-Broeck, Two-layer flows past a semicircular obstruction, Phys. Fluids **5**, 2661 (1993).
[14] S. S.-P. Shen, Forced solitary waves and hydraulic falls in two-layer flows, J. Fluid Mech. **234**, 583 (1992).
[15] F. Dias and J.-M. Vanden-Broeck, Steady two-layer flows over an obstacle, Philos. Trans. R. Soc. London A **360**, 2137 (2002).
[16] F. Dias and J.-M. Vanden-Broeck, Two-layer hydraulic falls over an obstacle, Eur. J. Mech. B/Fluids **23**, 879 (2004).
[17] R. R. Long, Some aspects of the flow of stratified fluids. II. Experiments with a two-fluid system, Tellus **6**, 97 (1955).
[18] P. G. Baines, A unified description of two-layer flow over topography, J. Fluid Mech. **146**, 127 (1984).
[19] G. A. Lawrence, The hydraulics of steady two-layer flow over a fixed obstacle, J. Fluid Mech. **254**, 605 (1993).
[20] P. F. Cummins, D. R. Topham, and H. D. Pite, Simulated and experimental two-layer flows past isolated two-dimensional obstacles, Fluid Dyn. Res. **14**, 105 (1994).
[21] C. Cabeza, J. Varela, I. Bove, D. Freire, A. C. Martí, L. G. Sarasúa, G. Usera, R. Montagne, and M. Araujo, Two-layer stratified flows over pronounced obstacles at low-to-intermediate Froude numbers, Phys. Fluids **21**, 044102 (2009).
[22] S. R. Belward and L. K. Forbes, Fully non-linear two-layer flow over arbitrary topography, J. Eng. Math. **27**, 419 (1993).

[23] T. R. Akylas, On the excitation of long nonlinear water waves by a moving pressure distribution, J. Fluid Mech. **141**, 455 (1984).
[24] L. J. Pratt, On nonlinear flow with multiple obstructions, J. Atmos. Sci. **41**, 1214 (1984).
[25] A. A. Chesnokov, S. L. Gavrilyuk, and V. Yu. Liapidevskii, Long nonlinear internal waves and mixing in a three-layer stratified flow in the boussinesq approximation, arXiv:2112.04756.